Geophysical Journal International

Geophys. J. Int. (2019) **218,** 2045–2053
Advance Access publication 2019 June 06
GJI Seismology

doi: 10.1093/gji/ggz262

Estimating lateral and vertical resolution in receiver function data for shallow crust exploration

Senad Subašić [1,2,3] Nicola Piana Agostinetti [4] and Christopher J. Bean[1]

[1] *Geophysics Section, Dublin Institute for Advanced Studies, Dublin 2, D02 Y006, Ireland. E-mail: senad@cp.dias.ie*
[2] *Irish Centre for Research in Applied Geosciences (iCRAG), University College Dublin, Belfield, Dublin 4, D04 V1W8, Ireland*
[3] *School of Earth Sciences, University College Dublin, Belfield, Dublin 4, D04 V1W8, Ireland*
[4] *Department of Geodynamics and Sedimentology, University of Vienna, 1090 Vienna, Austria*

Accepted 2019 June 4. Received 2019 May 10; in original form 2018 December 10

SUMMARY

In order to test the horizontal and vertical resolution of teleseismic receiver functions, we perform a complete receiver function analysis and inversion using data from the La Barge array. The La Barge Passive Seismic Experiment was a seismic deployment in western Wyoming, recording continuously between November 2008 and June 2009, with 55 instruments deployed 250 m apart—up to two orders of magnitude closer than in typical receiver function studies. We analyse each station separately. We calculate receiver functions and invert them using a Bayesian algorithm. The inversion results are in agreement with measurements from nearby wells, and from other studies using the same data set. The resulting posterior probability distributions (PPDs), obtained for each station, are compared to each other by computing the Bhattacharyya coefficients, which quantify the overlap between two PPDs. Our results indicate that (a) the lateral resolution of 8 Hz receiver functions is approximately equal to the width of their first Fresnel zone, (b) minimum investigable depth is about 400 m at 8 Hz, (c) lateral resolution depends on the local geology as expected and (d) velocity inversion in the shallow-crust can be resolved in the first few kilometres, even in case of dipping interfaces.

Key words: Statistical methods; Body waves; Crustal imaging.

1 INTRODUCTION

The structure of the shallow crust is of interest in many human activities, for example, geothermal, hydrocarbon and mineral exploration. Active seismic surveys provide an unparalleled view of the subsurface, but in areas where active surveys would be problematic (due to social, financial or geological reasons), passive seismic methods are an attractive alternative. Academic seismological methods using natural sources data, such as teleseismic receiver functions (RFs), widely used for crust and mantle studies, have been readily adapted for use on smaller scales and shallower structures (e.g. Liu *et al.* 2018; Piana Agostinetti & Martini 2019). Measurements of seismic ambient noise have been also used to investigate sedimentary basins (e.g. Lehujeur *et al.* 2018; Romero & Schimmel 2018).

The results obtained by these inherently lower resolution methods can provide independent constraints or additional information outside those furnished by active seismic studies. Teleseismic RFs have been a widely used tool in seismology over the past few decades, targeting prominent interfaces such as the Mohorovičić discontinuity or the lithosphere–astenosphere boundary, and for retrieving *S*-wave velocity models of the Earth's crust. Leahy *et al.* (2012) have shown that teleseismic RFs contain information at higher frequencies as well (up to 15 Hz), which makes them a viable option for studying the shallow crust. Some examples include Yeck *et al.* (2014), who constructed a sedimentary basin geometry map using 2 Hz RFs, and Zevallos *et al.* (2009), who jointly inverted magnetotelluric and 10 Hz RF data to find the basement depth in SE Brazil. Licciardi & Piana Agostinetti (2017) have applied RF methodology to a potential geothermal site in the Dublin basin, using a multifrequency approach, with frequencies up to 8 Hz. Piana Agostinetti *et al.* (2018) used RFs to map the basin-bounding fault in the Kenya rift, indicating that results obtained by the analysis of passive seismic data can be compared to those obtained with active seismics. While those studies demonstrate the potential of teleseismic RF data for shallow-crustal exploration, a detailed analysis of the uncertainties in the reconstructed surfaces and elastic models derived by those data is still lacking.

Here, we study uncertainties associated with RF analysis exploiting a freely accessible seismic archive containing 9 months of continuous recordings. A total of 55 closely spaced (250 m) broad-band seismic stations were deployed in Western Wyoming, perpendicular to a major local structural feature—the Hogsback thrust.

Given the non-linearity and non-uniqueness of the RF inverse problem, analytical estimates of uncertainties associated with RF analysis can be biased. We apply a Monte Carlo sampling scheme

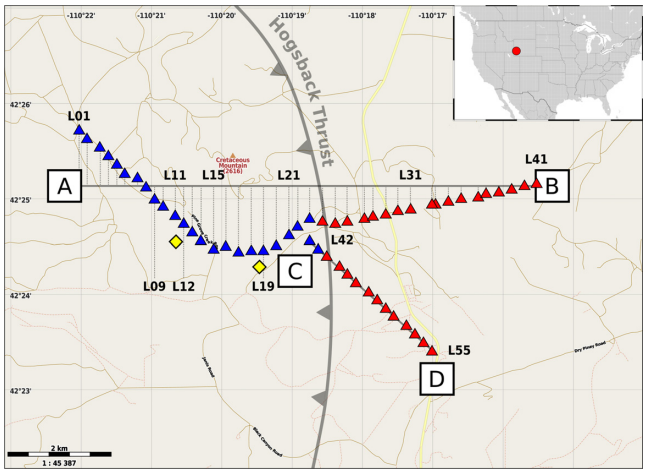

Figure 1. The LaBarge Passive Seismic Experiment array, adapted from Leahy *et al.* (2012). The interstation distance is roughly 250 m. Stations L01–L41 are projected on a linear profile AB, spanning approximately 9 km. The AB profile strikes perpendicular to the Hogsback thrust, a known geological feature of the area. Some stations are located near a highway and a gas pumping station, which influences the data quality. The yellow diamonds mark the approximate locations of wells. The blue and red triangles mark stations on the left-hand and right-hand side of the surface expression of the Hogsback thrust, respectively (referenced later in the text).

to obtain realistic uncertainties from Bayesian inferences. Sampling is performed via a trans-dimensional algorithm (Sambridge *et al.* 2006), in which the number of unknowns describing a model is treated as an unknown as well. For each station, we collect a full suite of velocity models using a reversible-jump Markov Chain Monte Carlo (RjMCMC) method (Green 1995; Malinverno 2002) and use the resulting ensemble of models for Bayesian inferences (e.g. to compute uncertainties on the investigated parameters). Trans-dimensional algorithms have a property of natural parsimony, that is, given a choice of two models that fit the data equally well, the simpler one will be preferred (see e.g. Malinverno 2000, 2002; Sambridge *et al.* 2006).

We empirically estimate vertical and lateral resolution of RF data by comparing results obtained from each station (analysed independently of the others) as a function of interstation distance. We compare our results with previous studies undertaken on the same data set, mainly with the work of Leahy *et al.* (2012), who performed RF analysis using frequencies up to 15 Hz. Other work includes studies by Behm *et al.* (2013), who determined surface wave velocities with ambient noise interferometry, and a local and regional tomography work by Biryol *et al.* (2013). The outline of this study comprises the analysis of each RF data set in terms of backazimuthal angular harmonics, the inversion of that data set using a Bayesian trans-dimensional algorithm and the computation of the Bhattacharyya coefficients (BCs) to measure the overlap of results between two stations. Outcomes of the analysis are discussed focusing on both the interstation distance and the depth of investigated interfaces.

2 DATA AND METHODS

We use data collected during the LaBarge Passive Seismic Experiment—an 8 month deployment in 2008 and 2009 in western Wyoming (see Saltzer *et al.* 2011; Leahy *et al.* 2012). We focus on the very dense part of the array, with 55 instruments installed 250 m apart on average (see Fig. 1). This passive seismic data set is freely downloadable from the International Research Institution

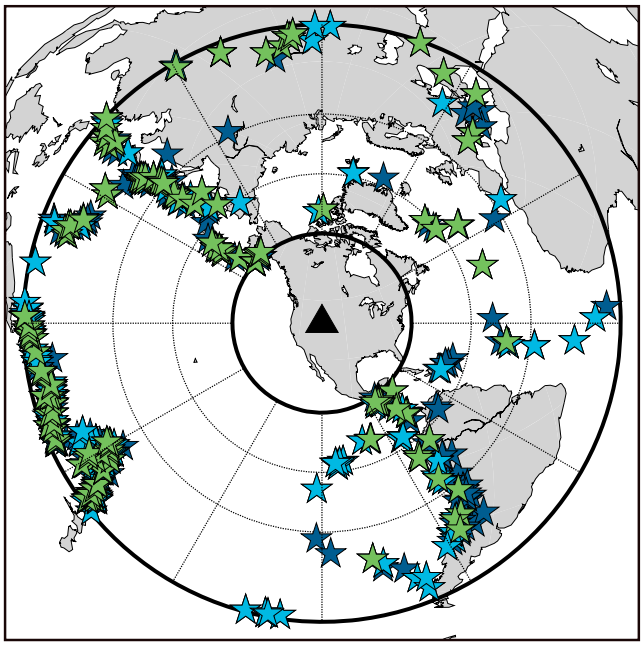

Figure 2. Distribution of earthquakes used to calculate receiver functions. Stars show all processed events, with the light blue stars showing events for which we obtained RFs, and the green stars showing good quality RFs selected for stacking and used in the inversion. The thick black circles mark the interval of interest—distances between 30 and 100° from the array, while the dotted circles and lines mark 30° bins in backazimuth and epicentral distances of 50 and 70°.

for Seismology (IRIS), and thus, it represents an optimal case study for investigating the resolution and uncertainties involved with RF imaging, guaranteeing the full reproducibility of our results.

We use teleseismic events with $M_W \geq 5.0$ that occurred between the 2008 November 1 and the 2009 June 9 at epicentral distances between 30 and 100°. For events less than 30° away from the receiver, the angle of incidence is no longer near-vertical. Beyond 100° the direct *P* arrival disappears. We choose to include relatively weak earthquakes in order to obtain a sufficiently large data set and adequate backazimuthal coverage from this relatively short deployment. Fig. 2 shows the events used. There is a gap between 170 and 230° in backazimuth, with very few or no events and poor quality RFs.

Seismograms are downsampled to 50 samples per second, and windowed to include 6 min of pre-signal noise and 1 min after the theoretical *P* arrival time, calculated using the TauP Toolkit (Crotwell *et al.* 1999) and the IASP91 velocity model (Kennett & Engdahl 1991). We calculate RFs using the frequency domain deconvolution method proposed by Bona (1998). This method estimates the pre-signal noise, and the noise involved in the deconvolution itself, both contributing to the uncertainty in the RFs. This approach enables us to calculate and interpret RFs from lower magnitude events as well, and greatly increase our data set—half of the total number of good quality RFs we use is obtained from earthquakes with $M_W \leq 5.5$. RFs are filtered using a Gaussian filter with a 90 per cent cut-off at 8 Hz (Gaussian parameter a = 16), chosen based on the coherency of resulting RFs between stations. We sort the resulting RFs with respect to backazimuth, and visually check and select only good quality ones (pronounced initial *P* arrival at 0 s, limited ringing in the acausal portion or in the averaging function, good coherence with other RFs from similar backazimuths). Good backazimuthal coverage is very important here, as it helps

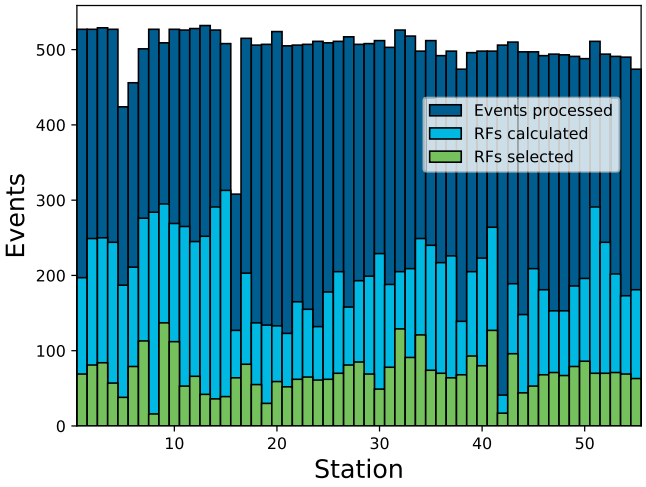

Figure 3. Number of processed events, and calculated and selected 8 Hz receiver functions at each station. Some stations have fewer recorded or usable events due to noise or missing data.

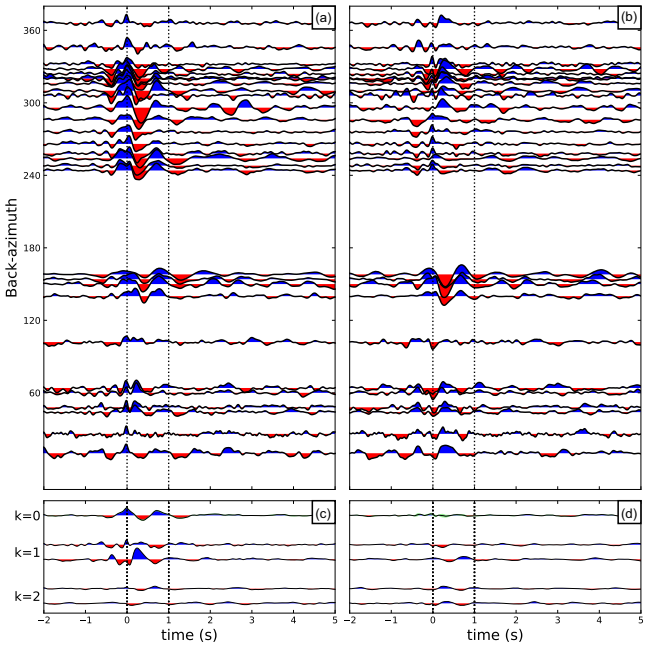

Figure 4. (a) Radial and (b) transverse receiver function stacks used in harmonic decomposition at station L09. The blue and red pulses correspond to positive and negative amplitudes, respectively. Note the two-lobed pattern in panels (a) and (b) between 0.3 and 0.5 s (see main text for details). Panels (c) and (d) show the modelled (c) and unmodelled (d) combined harmonics of order k = 0, 1 and 2. The modelled components enhance effects of dipping or anisotropy, while the unmodelled components are mainly influenced by scattering and 3-D heterogeneities (for details, see e.g. Bianchi *et al.* 2010b). The E–W harmonic dominates the modelled components, which indicates the presence of a dipping interface striking predominantly E–W—consistent with known structures.

distinguish pulses generated at actual interfaces from random correlations found in the noise. We look for coherent pulses present in waveforms at different backazimuths. Fig. 3 shows a breakdown of the number of events and RFs obtained.

We sort the RFs into bins (10° in backazimuth and 20° in epicentral distance; see Fig. 2), and calculate a weighted stack of all RFs in their respective bins. The weights are the inverse of the variance of the RFs, defined in appendix A of Bona (1998). We perform harmonic decomposition of our RF data set (see e.g. Shiomi & Park 2008; Bianchi *et al.* 2010b) to separate contributions from isotropic and anisotropic or dipping structures. This process consists of solving a linear system of equations using radial and transverse RF at each sample point to retrieve the harmonic coefficients. The RF data set is represented as a weighted sum of $\sin(k\phi)$ and $\cos(k\phi)$ terms, where $k = 0, 1, 2$ is the harmonic order, and ϕ is the backazimuth. The presence of an anisotropic layer or a dipping velocity contrast is revealed by the variations of amplitudes and polarities of RF pulses in backazimuth. A two-lobed pattern (or 2π periodicity) is generated by a dipping velocity discontinuity or a layer with hexagonal anisotropy and a dipping symmetry axis. A four-lobed pattern (or π periodicity) appears in the presence of a layer with hexagonal anisotropy and a horizontal symmetry axis. These patterns can be enhanced or diminished by summing up the radial and transverse RFs with a 'phase shift' in backazimuth—a phase shift of $\pi/2k$, usually denoted as the 'modelled' component, enhances the periodic patterns; a phase shift of $-\pi/2k$ (the 'unmodelled' component) results in destructive interference of the patterns, leaving behind signatures of scattering or complex 3-D structures (see Shiomi & Park 2008; Bianchi *et al.* 2010b; Park & Levin 2016). Fig. 4 shows an example of harmonic decomposition of RFs at station L09, where a two-lobed pattern can be easily identified. There is a pronounced negative (red) arrival at 0.3–0.5 s in the radial RF stacks (Fig. 4a), with amplitudes and delay times depending on the backazimuth. The negative arrival is less clear for backazimuths between 0 and 100°. Transverse RF stacks show a polarity change with backazimuth at 0.3–0.5 s, with minimal amplitudes at approximately 260°.

Zero-order harmonics are the input for RF inversion. The forward solver used is the Thomson–Haskell matrix method (Thomson 1950; Haskell 1953) that calculates the response of a stack of horizontally homogeneous and isotropic layers. Such long-standing method has been widely used for Monte Carlo studies due to its very limited computation time (e.g. Shibutani *et al.* 1996).

The inverse problem is solved in a Hierarchical Bayes framework, where the final result consists of an ensemble of models collectively defining the posterior probability distribution (PPD) that describes the subsurface given the prior information (prior probability distribution) and the data (likelihood, i.e. the probability of observing the data d given a certain model m and prior information I). Hierarchical Bayes approach implies having loose prior information on the uncertainties on the data, which are also considered part of the investigated parameters (Malinverno & Briggs 2004; Bodin *et al.* 2012). Here, each model is composed by a variable number of parameters: (1) a scalar k representing the number of interfaces in the model; (2) a k-vector containing the depths of the interfaces; (3) two $k + 1$-vectors containing the S-wave velocity and V_P/V_S ratio of each layer defined between two interfaces, and of the underlying half-space and finally (4) a scalar π used to modulate the data uncertainties. Models from the PPD are sampled by a trans-dimensional algorithm, so-called reversible jump Markov Chain Monte Carlo (RjMCMC), developed by Piana Agostinetti & Malinverno (2010, 2018), in which the number of layers is considered as an unknown parameter. The main advantage of the trans-dimensional approach is that the model complexity is inferred directly from the data. At each step of the Markov chain, a candidate model is proposed, based on a perturbation of the current model. Here, the current model is randomly perturbed selecting one of five different moves. In the first move, the parameter π is perturbed, allowing to investigate the data uncertainties; the second move implies the perturbation of the

S-wave velocity and V_P/V_S ratio profiles; the third move produces a perturbation of the depth of one interface; the fourth and fifth moves are the so-called 'trans-dimensional moves' because they consider adding or removing one interface and, thus, modifying the dimensionality of the model.

In this study, we follow the workflow depicted in Mosegaard & Tarantola (1995) for sampling the PPD, which uses a simplified Metropolis' rule. First, a candidate model is selected according to the prior information. In the second step, such candidate is accepted or rejected with probability:

$$\alpha = \min\left[1, \frac{L(m_{\text{cand}})}{L(m)}\right], \tag{1}$$

that is, the Metropolis' rule, where $L(m_{\text{cand}})$ and $L(m)$ are the likelihood functions for the current and candidate model, respectively. If the likelihood of the candidate model is larger than that of the current model, the candidate is always accepted. Otherwise, the candidate is accepted with a probability equal to α. Thus, models that worsen the fit to the data can also be accepted along the chain, depending on how much the fit has deteriorated. The likelihood function is given by

$$p(\mathbf{d}|\mathbf{m}, \mathbf{I}) = \frac{1}{\sqrt{[2\pi^N|\mathbf{C_e}|]}} \exp\left(-\frac{1}{2}\mathbf{e}^{\mathbf{T}}\mathbf{C_e^{-1}}\mathbf{e}\right), \tag{2}$$

where $e_i = (d_i - p_i)$ is the vector of residuals between data and predictions, and $\mathbf{C_e}$ is the covariance matrix representing the statistics of data errors. The covariance matrix can be expressed as

$$\mathbf{C_e} = \mathbf{SRS}, \tag{3}$$

where $\mathbf{S}$ is a diagonal matrix with the standard deviations along the main diagonal, and $\mathbf{R}$ is a correlation matrix (as defined in Piana Agostinetti & Malinverno 2010). Due to the empirical correlation matrix being numerically unstable in our case (likely due to the limited number of selected RFs per station), we instead use a Gaussian correlation matrix (see appendix D in Bodin *et al.* 2012). In detail, we use the uncertainties estimated on each k = 0 harmonic through a bootstrap approach (e.g. Bianchi *et al.* 2010b) as the element of matrix $\mathbf{S}$, and a Gaussian correlation matrix with a fixed decay coefficient equal to R = 0.945. In this case, the noise correlation between data-points that are i samples apart is represented by

$$c_i = R^{i^2}. \tag{4}$$

A Gaussian correlation matrix is continuous and differentiable along the main diagonal and an analytical representation of its inverse is not available. Thus, we approximate its inverse using singular value decomposition. We refer the reader to Dettmer *et al.* (2015) for a discussion on different likelihood functions for Bayesian inversion of teleseismic data.

3 RESULTS

We identify a pronounced negative arrival between 0.3 and 0.5 s in the radial RF stacks at station L09 (Fig. 4a). The amplitude and delay time of this negative pulse display backazimuthal variation, indicating dipping or anisotropy. This is accompanied by a polarity change in the transverse RF stacks in the same time interval (Fig. 4b).

Plotting the zero-order harmonic obtained at all stations in the array, shown in Fig. 5, reveals a pattern. The aforementioned pronounced negative pulse is present only at stations L01–L15, and appears earlier in time moving from A to B (or west to east). This

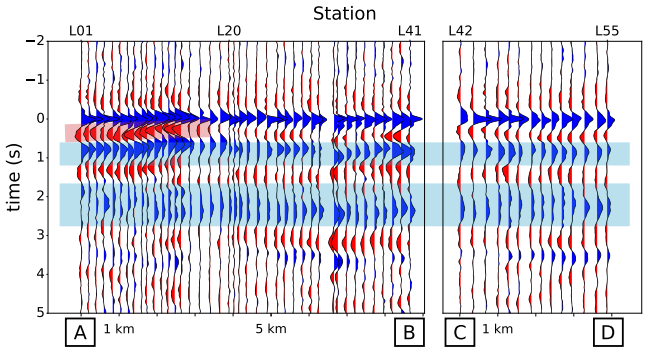

Figure 5. Zero-order harmonics, plotted at projected locations along the AB and CD profiles (Fig. 1). Stations L01–L15 show a pronounced negative (red) arrival in the first 1 s. This negative arrival appears earlier as we move from west to east along the profile, indicating a dipping low-velocity structure. The blue arrival at 0.8–1 s is a primary conversion on an interface present across the array. The positive arrivals between 2 and 3 s are interpreted as its multiples (see Leahy *et al.* 2012).

is another indication of a dipping interface, in agreement with the backazimuthal variations in radial and transverse RF stacks at a single station from Fig. 4. However, in this paper we consider only the zero-order harmonics at individual stations, and do not use the information on dip or anisotropy in our inversion.

We run the 1-D RjMCMC RF inversion using 300 000 models (100 000 model burn-in phase) and 92 independent chains, for a total of 27.6×10^6 models per station. This is the length needed to reach convergence in the chains as found in preliminary tests. Each model is characterized by the number of interfaces, their depths and the elastic parameters of each layer. The prior consists of normal distributions for the *S*-wave velocity and V_P/V_S ratios, with means and standard deviations defined in 100 m intervals (see Table 1 in the Supporting Information). We impose uniform distributions for the number of layers (between 1 and 100), and interface depths (between 0 and 60 km, with a minimum interface thickness of 100 m). We follow the approach outlined by Mosegaard & Tarantola (1995) in which the prior distribution does not need to be defined by an explicit formula. To demonstrate that the proposed models are distributed as in the prior distribution, we run the algorithm with the likelihood set to 1. The results are shown in Fig. 1 in the Supporting Information and confirm the reliability of our algorithm. We set tight constraints on the velocity in the top two layers (top 200 m) to avoid unrealistically high velocities in these shallowest parts where we do not have the required resolution. Below 200 m the prior is loosely constrained, with a standard deviation decreasing linearly with depth. We account for the large variability near the surface with a standard deviation of 500 m s^{-1} at 300 m. As this variability decreases (generally up until the Moho, see e.g. Christensen & Mooney 1995), the standard deviation at the bottom of the model (at the depth of 60 km) is set to 200 m s^{-1}. This depth-dependent prior has been used elsewhere (e.g. Bianchi *et al.* 2010a; Amato *et al.* 2014); it represents a more realistic description of the subsurface, and the slow change in the standard deviation with depth has little effect on the output for the shallowest layers. Inversion results are expressed in terms of marginal PPDs of the parameters of interest (e.g. V_S, number of interfaces, interface depths and so on). The resulting marginal PPDs of selected parameters for station L15 are shown in Fig. 6 (plots for other stations can be found in the Supporting Information). The negative pulse from Fig. 5 resolves to a velocity inversion zone between 600 m and 2 km in depth (at L15). The *S*-wave velocity drops from 2.6 to 2.0 km s^{-1}, levelling off around

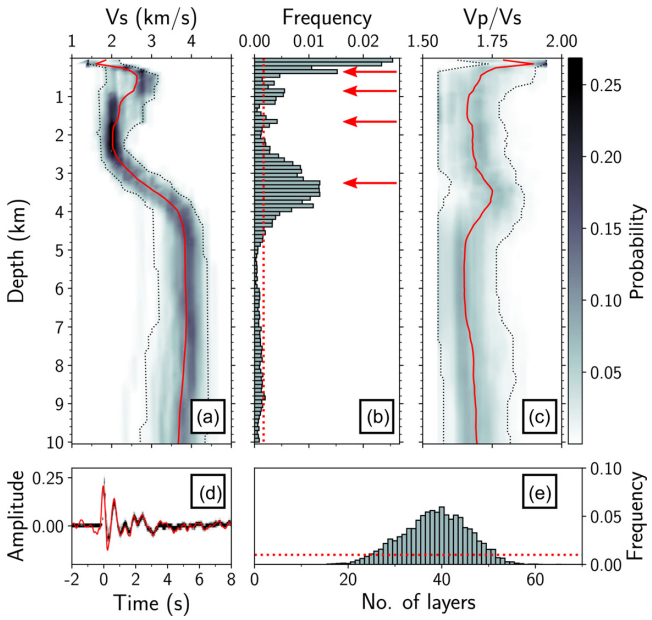

Figure 6. Receiver function inversion results: example for station L15; (a) density plot of marginal posterior probability distribution of *S*-wave velocity, with the mean *S*-wave velocity plotted as a solid red line, and 95 per cent credible intervals plotted as the dotted black lines; (b) histogram of interface depths in the sampled models, with the red arrows pointing to four most pronounced maxima (high probabilities of interfaces at those depths); (c) PPD for the V_P/V_S ratio, with the mean plotted as a solid red line, and 95 per cent credible intervals as the dotted black lines; (d) fit between observed (red) and posterior RF; (e) histogram of the number of layers in the sampled models. The dotted red lines in panels (b) and (e) represent the uniform probabilities for the interfaces and number of layers, respectively.

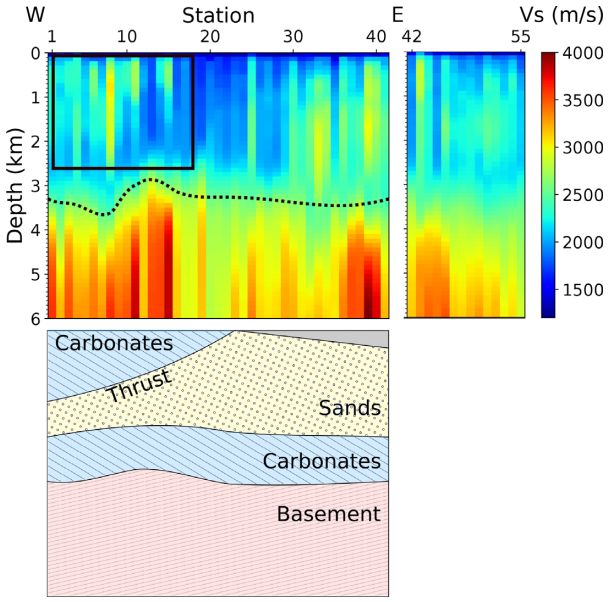

Figure 7. Top: receiver function inversion results—mean posterior *S*-wave velocity model, plotted to a depth of 6 km; the negative arrival shown in Fig. 4 resolves to a velocity inversion layer starting from 200 to 300 m and reaching up to 2.5 km in depth in the westernmost part of the array, thinning out towards the east and disappearing around station L16 (highlighted by a black rectangle). Variation in basement depth is also well resolved (the black dotted line). The horizontal and vertical scales are approximately equal. Bottom: schematic of the thrust, adapted from Leahy *et al.* (2012).

2 km in depth. There is a gradual increase between 2.5 and 4 km, with the velocity attaining a maximum value of close to 4 km s^{-1}. It should be noted that RFs are most sensitive to velocity contrasts, and not absolute velocities. They can only constrain a combination of the velocity above and depth to an interface (e.g. Ammon *et al.* 1990; Kind *et al.* 1995). This is apparent in the most prominent feature of Fig. 6(b)—a diffuse boundary between 2.5 and 4 km in depth. Other notable interfaces are the top of the high-velocity layer (most probable depth of 400 m, with $V_S \approx 2.6$ km s^{-1}), followed by the velocity inversion zone with two less pronounced interfaces at around 900 and 1600 m, where the velocity drops to $V_S \approx 2$ km s^{-1}. Below that we have the aforementioned diffuse boundary, and a gradual increase to $V_S \approx 4$ km s^{-1} between 2.5 and 4 km in depth. This corresponds to the wide blue pulse at ∼0.7 s delay time in Fig. 5. The dotted black lines in Figs 6(a) and (c) denote the 95 per cent credible intervals. Posterior uncertainty for L15 is lowest (credible intervals are narrowest) around 2.2 km depth, where the velocity inversion ends. Similar behaviour is observed at virtually all stations in the array (see inversion result figures in the Supporting Information), with minimum uncertainty (for the top 10 km shown) at the start of the large velocity gradient (between 2 and 3 km depth). There is a good agreement between the observed and posterior RFs (Fig. 6c), that is, the resulting velocity model accurately reproduces the data retrieved at the station. The V_P/V_S ratio is poorly constrained, with very wide credible intervals. As generally noted in RF studies, V_P/V_s ratio estimates should only be considered collectively as regional estimates (e.g. Licciardi & Piana Agostinetti 2014).

The resulting mean posterior *S*-wave velocity model is shown in Fig. 7. The negative arrivals from Figs 4 and 5 resolve to a velocity inversion starting from approximately 2–3 km in depth in the westernmost part of the array, and getting gradually shallower towards the east. The blue pulses highlighted in Fig. 5 are generated on the top of the basement. The depth of this interface is between 3 and 4 km, showing smooth variation from station to station.

4 DISCUSSION

A pronounced negative arrival in Fig. 4 is present for backazimuths between 140 and 330°, at 0.3–0.5 s. The amplitudes and delay times of these pulses show backazimuthal variation, which is an indication of structural dip or anisotropy. The largest amplitudes of the negative pulse appear at approximately 290°. Largest amplitudes are obtained for incident waves traveling up-dip (see e.g. Cassidy 1992), which would in this case indicate a west dipping interface—most likely corresponding to the Hogsback thrust (see Leahy *et al.* 2012). We can identify a two-lobed pattern in the transverse receiver function (TRF) amplitudes, consistent with a dipping interface, at 0.3–0.5 s. TRF amplitudes are close to zero for traces arriving from approximately 260° backazimuth, which indicates either the direction of dip, or the direction opposite. Even though there is a backazimuthal gap between 60 and 100°, we can safely pick 260° as the approximate dip direction, due to the radial receiver function amplitudes in Fig. 4(a) being much larger around 260° than at either 60 or 100°. The 'unmodelled' components in Fig. 4(d) show limited energy, which indicates that the effects of complex geometries, heterogeneities, scattering or poor backazimuthal coverage are in this case minimal. We can, therefore, point out the presence of a west-dipping interface in the westernmost end of the profile.

The bottom of the sedimentary basin is not resolved as a sharp transition, but it seems to be a gradational boundary, as seen in Figs 6(a) and (b). However, we cannot rule out that the gradational

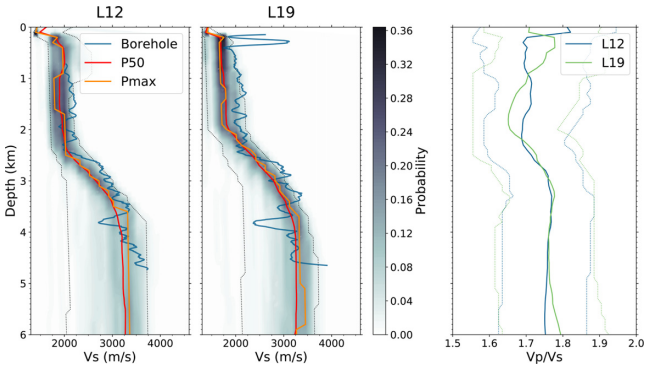

Figure 8. Comparison of RF inversion results at stations L12 (left) and L19 (centre) with data from nearby boreholes (the blue lines). Plotted are V_S PPDs (the grey shading), 95 per cent credible intervals (the dotted black lines), median (the red line) and Pmax (the orange line) values of the PPDs. Right: mean V_P/V_S ratios and the 95 per cent credible intervals. V_P borehole data were digitized from Leahy *et al.* (2012), and converted to V_S by dividing it by the posterior mean V_P/V_S ratio. We apply a third-order Savitzky–Golay filter with a window size of approximately 200 m. P50 and Pmax values of V_S PPDs are slightly lower than the V_S estimated from borehole data, but the velocity gradient and basement depth are well matched at both stations. RFs filtered at 8 Hz are unable to capture the high-velocity variations in the top 500 m at L19.

nature of the transition from sediments to basement is given by the trade-off between depth and velocity (given by the fact that models with a high *S*-wave velocity in the sediments and a deeper interface fit equally well to models with slower sediments and a shallower interface), as pointed out in, for example, Licciardi & Piana Agostinetti (2016). Even though the basement boundary is not sharply defined, we do resolve some topography. We find smooth variations in depth (Fig. 7), mostly confined to the westernmost end of the array, below the Hogsback thrust. This result is very similar to the structural model used for forward calculations obtained by Leahy *et al.* (2012).

We have the opportunity to compare our posterior velocity model with data from nearby wells. The wells are located near stations L12 and L19 (see Fig. 1). We use the borehole V_P data from Leahy *et al.* (2012), and convert them to V_S using the posterior V_P/V_S ratio from the inversion. Fig. 8 shows the comparison between the converted borehole data and the mean posterior V_S obtained from our inversion. Our mean posterior V_S is systematically slower than the V_S estimated from borehole data. However, the agreement between RF and borehole data is otherwise good, with both the depth of the basement and the velocity gradient matching well at both stations. The absolute velocity difference is, therefore, likely a consequence of our crude conversion from V_P to V_S, as the posterior V_P/V_S ratio has very wide credible intervals at all depths. The velocity variation in the top 300–400 m at L19 could not be resolved with either 8 or even 12 Hz RF data.

In order to estimate the horizontal and vertical resolution of the RF methodology, we need to quantify the similarities between PPDs obtained at different stations. We have opted for the BC as the measure of the amount of overlap. For two normalized discrete distributions $\mathbf{p}$ and $\mathbf{q}$, BC is defined as $\mathrm{BC}(\mathbf{p},\mathbf{q}) = \sum_{i=1}^{n} \sqrt{p_i q_i}$, where n is the number of partitions, and p_i and q_i are the probabilities in the ith partition. BC values range from 0 (no overlap) to 1 (matching distributions).

Fig. 9 shows an example of the BC calculated between PPDs for two adjacent and two distant stations. At a fixed depth of 2 km, the PPDs of adjacent stations are nearly identical, resulting in a BC

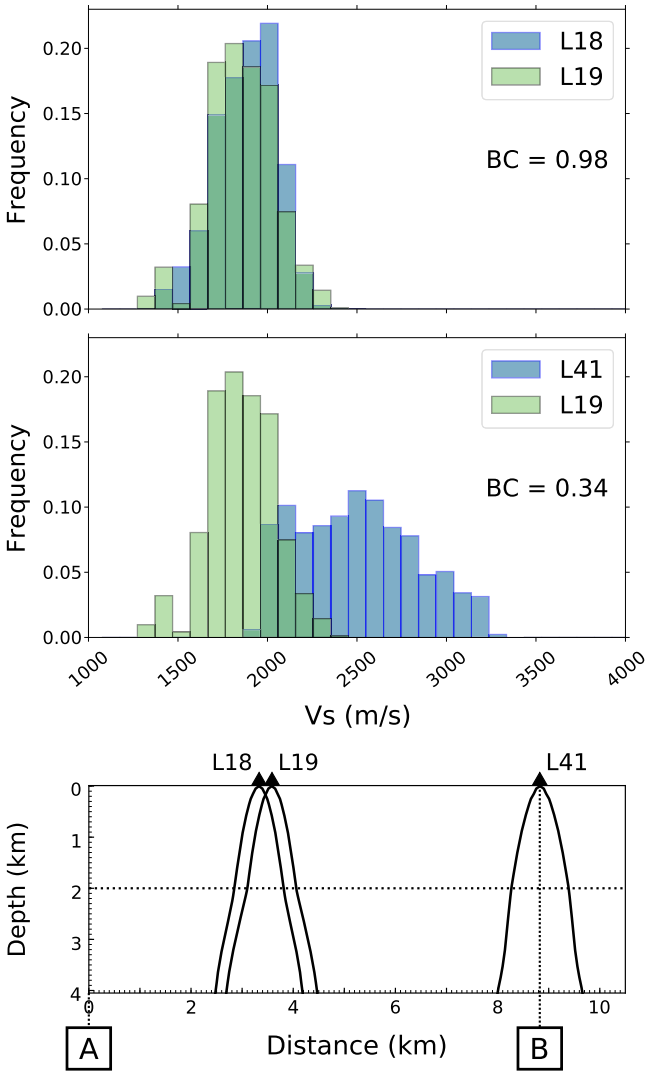

Figure 9. Marginal posterior probability distributions of V_S at the depth of 2 km. Top and middle: two adjacent stations, L18 and L19, 250 m apart, have very similar distributions, and a high value of the Bhattacharyya coefficient (BC). Bottom: two distant stations, L19 and L41, 5.5 km apart, have disjointed distributions and a low BC value. Bottom: sketch of the 8 Hz Fresnel zones at the same stations. The dotted line highlights the depth of 2 km, used in the histograms above. A and B are the profile markers used in Fig. 1.

close to unity. These stations sample virtually the same structure at 2 km in depth. Two distant stations at this depth have very different PPDs, and, therefore, a very low BC value. Their Fresnel zones are completely separated, and they sample different structures.

We calculate the BC between all station pairs in the array, resulting in 1485 BCs at every depth level (in 100 m intervals). We sort the BCs by interstation distance, using 250 m bins, and calculate the average of each bin. The resulting BC variation with interstation distance and depth is shown in Fig. 10. Average BC values and coherency between stations increase going from shallow to deep crust. For shallow depths (500 m), the coherence between stations more than 2 km apart is low, but geological heterogeneity could compromise coherency even for closer stations. This is very apparent in Fig. 11, where we calculate average BCs between station pairs on either side of the surface expression of the Hogsback thrust separately. We see clear differences between stations on the left-hand and right-hand side of the Hogsback thrust. Very

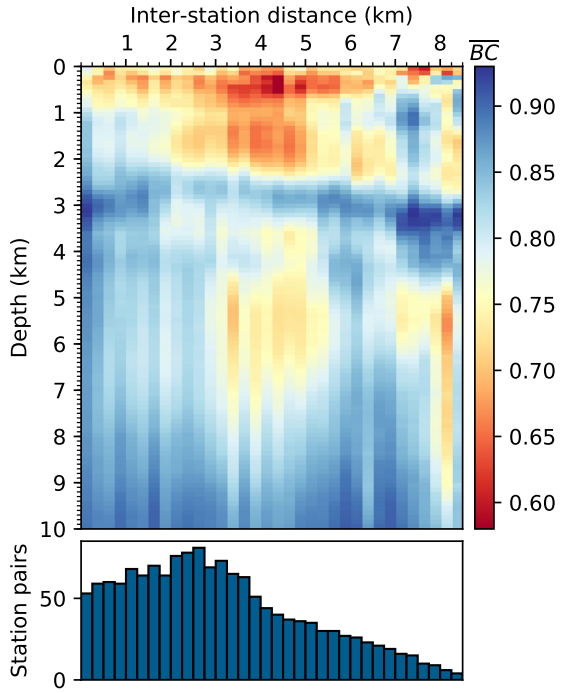

Figure 10. Top: plot of the Bhattacharyya coefficient (BC) with respect to interstation distance and depth (see text for details); bottom: number of station pairs at different interstation distances, bins set to 250 m. This plot includes inversion results and real (not projected) interstation distances for stations L01–L55 (both AB and CD profiles). For the shallowest sections, BC is low—implying lateral heterogeneities—even for adjacent stations. Coherence improves after 500 m in depth, and diminishes with distance. At the depth of 3 km, BC is large at all interstation distances—stations at various distances share a similar V_S PPD, implying they sample the same structure (the basement).

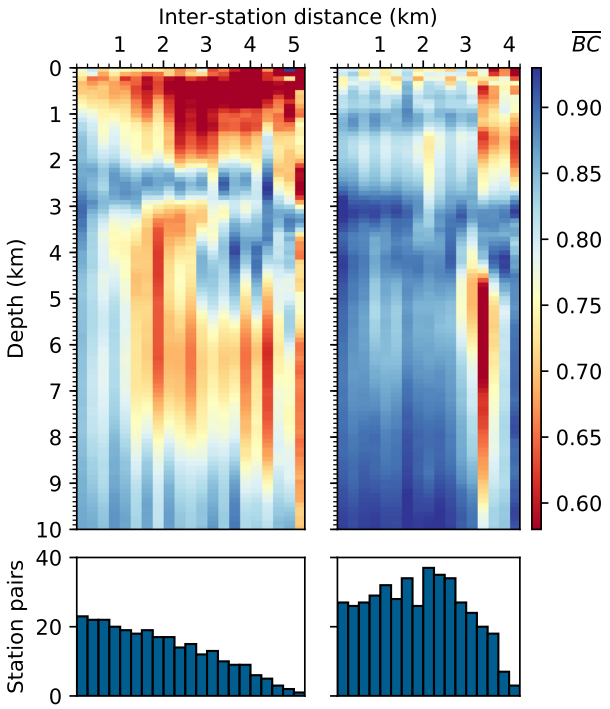

Figure 11. Same as Fig. 10, except here we separate stations on the left of the surface expression of the Hogsback thrust from the ones on the right. Stations on the left image the thrust itself, an area of high lateral heterogeneity, which results in a significant drop in $\overline{BC}$ values at shallow depths. Stations on the right-hand side of the thrust show a remarkable coherence at all depths and interstation distances. Colour scale is the same for both plots, and for the plot in Fig. 10.

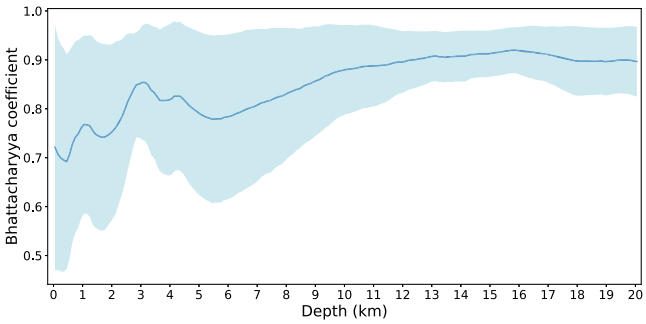

Figure 12. Average Bhattacharyya coefficient as a function of depth. The solid blue line is the mean value of BCs calculated for all station pairs, with the standard deviation shown as the light blue shading. The largest discrepancies are in the shallowest parts, decreasing gradually until the top of the basement. The mean BC increases with depth.

high lateral heterogeneity on the left-hand side, with low average BC values between adjacent stations. Stations to the right of the thrust are coherent at nearly all depths and interstation distances. Another notable feature of Fig. 10 is a localized minimum in average BC values at around 6 km in depth for stations between 3 and 6 km apart. Inversion results at stations in the middle (L17–L24, and L25–L35 to a lesser degree; see Supporting Information) show a lower mean posterior V_S at these depths, compared to stations at either end of the array. 3.5–5.5 km is also roughly equivalent to the distance between pairs of stations that are almost guaranteed to be located on opposite sides of the thrust, which will also contribute to a lower average BC. Average BCs attain a local maximum at all interstation distances at around 3 km in depth. This can be explained by the presence of the basement, retrieved at all stations in the array. The majority of sampled models agree on the depth and velocity PPDs at this interface, adding up to a very high average BC. The maximum average BC is slightly lower and located at shallower depths for interstation distances between 2 and 4 km. This is a consequence of the basement topography, with the depth starting to change around L08 (located 1.7 km away from L01)—several station pairs at distances larger than 1.7 km place the basement at different depths, resulting in a lower average BC value. Maximum average BC values increase again and shift back down to 3 km in depth for stations more than 5 km apart. This is essentially a moving average, with interstation distances representing the box width. Short interstation distances are sensitive to small-scale variations in interface depths, while larger distances (5 km or more in this case) smooth those variations out.

In Fig. 12, we plot the average BC values between all station pairs with depth. The standard deviation (the blue shading) is largest in the shallow parts due to lateral heterogeneities between different station pairs. The spread decreases with depth, until we hit the basement at around 3 km. Virtually all station pairs see an interface here, resulting in high individual BC values and consequently in high average BC. However, we notice significant deviations from the average for stations L11–L15 and L19–L22 around basement level (between 3 and 4 km in depth, see inversion results in the Supporting Information). This is due to basement topography, and the larger spread

in posterior interface depths at stations situated above the Hogsback thrust (the blue dots in Fig. 57 in the Supporting Information). The agreement between different station pairs decreases again and hits a local minimum at around 6 km in depth. Overall, average BCs (and standard deviations) increase (decrease) with depth, as expected.

A large number of stations in the middle and easternmost parts of the array (L23–L55) have a high BC value (>0.8, and even 0.9) at all depths. PPDs obtained at stations located on the eastern side of the Hogsback thrust (stations marked in red in Fig. 1) are very similar to each other, as shown in Fig. 11. The number and coherence of these stations are a major component in determining the average PPD, which explains the BC values between these individual PPDs and the average one being large at all depths. Similarly, the area overlying the Hogsback thrust is the more complex section of the array, with large discrepancies of individual station's V_S PPDs from the average. There is a lower number of stations in this area, and they are not as coherent, so they do not have a major influence on the average PPD. Below 6 km, BC converge again, with the average value reaching 0.9 at around 12 km in depth. The focus of this work is in the shallow crustal structure, but it is interesting to note that average BC stays above 0.9 from 12 km until approximately 40 km in depth (see Supporting Information). Increased scatter and a decrease in average BC below 40 km might be a signature of the Moho (which various studies place between 35 and 45 km in depth; e.g. Bensen *et al.* 2009; Mooney & Kaban 2010; Leahy *et al.* 2012). A clear and coherent Moho arrival was not present in our data set, so there will be differences between stations—some might include a weak or diffuse interface in their PPDs at that depth, some might not, leading to increased scatter of BC values.

Lateral resolution is generally taken to be equal to the width of the first Fresnel zone; a roughly circular area at an interface in which the signal interferes constructively (illustrated in Fig. 9). We infer the lateral resolution of 8 Hz RFs at each individual station by looking at the BCs with respect to interstation distance. From Fig. 11, we can see that, on average, PPDs of adjacent stations in the laterally heterogeneous part of the array (left of the thrust) become similar ($\overline{\mathrm{BC}} \geq 0.8$) after 800 m in depth. Above 800 m, adjacent stations see different structure, and closer station spacing (or higher frequency data) would be needed to recover shallower structure. Below 1 km in depth, the cone or rather triangle-shaped area obtained by connecting points with $\overline{\mathrm{BC}} \approx 0.8$ in Fig. 11 approximates the theoretical width of the first Fresnel zone fairly accurately. For example, if we were interested in sampling a structure at 1.6 km in depth, we find that stations up to 1 km apart have very similar PPDs there. In this simple scenario, where each station is analysed independently of others, installing stations at less than 1 km spacing would not yield any additional information at this depth. However, consistent results between neighbouring stations would provide a check on data quality. The basement appears to be homogeneous across the array, with high average BC values at all interstation distances. Below the basement, average BC drops for stations more than 1.25 km apart. So, for investigating depths between 2 and 10 km using 8 Hz RFs, station spacing of 1 km seems to be adequate. The first approximation of vertical resolution is the dominant wavelength. For 8 Hz RFs, and a velocity of 2000 km s^{-1}, this is equal to 250 m. This explains why we are unable to detect the high-velocity variations near the surface in Fig. 8. We can detect the presence of a low-velocity layer (due to the Hogsback thrust, with Palaeozoic carbonates being emplaced above late Mesozoic clastics; see Biryol *et al.* 2013 and references therein) up to 400 m in depth at station L15 (Fig. 6). We also resolve two distinct interfaces at 400 and 800 m in depth at the same station, so we estimate the vertical resolution to be at least 400 m.

5 CONCLUSIONS

We present inversion results and uncertainties involved with high frequency teleseismic RF data obtained from a temporary deployment with very dense station spacing. This enables us to investigate the horizontal and vertical limits of the RF methodology. We identify structural features in the top 3–4 km, including a dipping low-velocity structure, interpreted as a signature of the Hogsback thrust. This dipping structure and the corresponding velocity inversion is identifiable on stations L01–L15. RjMCMC inversion of 8 Hz RFs places the thrust at approximately 300 m depth at station L15, with an estimated thickness of 400 m. To resolve it beyond that, we would need to use higher frequencies—12 Hz RF data at the adjacent station (L16) again shows a signature of the velocity inversion. Therefore, we estimate the vertical resolution to be at least 400 m. We perform a statistical analysis of the marginal PPDs of *S*-wave velocity and find that the lateral resolution of 8 Hz RFs is approximately equal to the width of their first Fresnel zone—stations 250 m apart yield different estimates of the elastic parameters in the top 200 m. The bottom of the basin is also well resolved and coherent across the array. Since we consider each station independently, this is another indication of the robustness of the inversion. The agreement between V_P from well logs and our results is very good—the absolute differences being attributed to the crude conversion from posterior V_S to V_P. The posterior velocity uncertainties are smallest in the shallowest sections, and around basement depth (approximately 200–300 m s^{-1}). Simultaneously inverting RFs filtered using different cut-off frequencies (highlighting features at different scales) provides more accurate estimates, better constraining both interface depths and absolute values of V_S (Piana Agostinetti & Malinverno 2018). We demonstrate that high-frequency RFs are well suited for shallow crustal imaging, either as a complement or an alternative to other geophysical methods. Achievable resolution depends on the choice of frequencies used, which is in turn influenced by site conditions and deployment length and geometry.

ACKNOWLEDGEMENTS

We thank the editor Frederik Simons, an anonymous reviewer, and Anandaroop Ray for their comments and suggestions on improving the quality of the manuscript. This publication has emanated from research supported in part by a research grant from the Science Foundation Ireland (SFI) under grant numbers 13/RC/2092 and 14/IFB/2742, and is co-funded under the European Regional Development Fund. NPA's research is funded by Austrian Science Fund (FWF) under grant number M2218-N29. All support is gratefully acknowledged.

The facilities of IRIS Data Services, and specifically the IRIS Data Management Center, were used for access to waveforms, related metadata and/or derived products used in this study. IRIS Data Services are funded through the Seismological Facilities for the Advancement of Geoscience and EarthScope Proposal of the National Science Foundation under Cooperative Agreement EAR-1261681.

This work has been carried out using the ResearchIT Sonic cluster that was funded by UCD IT Services and the Research Office.

Some figures were created using the Generic Mapping Tools software package (Wessel *et al.* 2013). Map data copyrighted OpenStreetMap contributors and available from https://www.openstreetmap.org/ under the Open Database Licence.

REFERENCES

Amato, A., Bianchi, I. & Agostinetti, N.P., 2014. Apulian crust: top to bottom, *J. Geodyn.,* **82,** 125–137.

Ammon, C.J., Randall, G.E. & Zandt, G., 1990. On the nonuniqueness of receiver function inversions, *J. geophys. Res.,* **95**(B10), 15 303–15 318.

Behm, M., Leahy, G.M. & Snieder, R., 2013. Retrieval of local surface wave velocities from traffic noise—an example from the La Barge basin (Wyoming), *Geophys. Prospect.,* **62**(2), 223–243.

Bensen, G.D., Ritzwoller, M.H. & Yang, Y., 2009. A 3-D shear velocity model of the crust and uppermost mantle beneath the United States from ambient seismic noise, *Geophys. J. Int.,* **177**(3), 1177–1196.

Bianchi, I., Chiarabba, C. & Piana Agostinetti, N., 2010a. Control of the 2009 L'Aquila earthquake, central Italy, by a high-velocity structure: a receiver function study, *J. geophys. Res.,* **115**(B12).

Bianchi, I., Park, J., Piana Agostinetti, N. & Levin, V., 2010b. Mapping seismic anisotropy using harmonic decomposition of receiver functions: an application to Northern Apennines, Italy, *J. geophys. Res.,* **115**(B12).

Biryol, C.B., Leahy, G.M., Zandt, G. & Beck, S.L., 2013. Imaging the shallow crust with local and regional earthquake tomography, *J. geophys. Res.,* **118**(5), 2289–2306.

Bodin, T., Sambridge, M., Gallagher, K. & Rawlinson, N., 2012. Transdimensional inversion of receiver functions and surface wave dispersion, *J. geophys. Res.,* **117**(B2).

Bona, M., 1998. Variance estimate in frequency-domain deconvolution for teleseismic receiver function computation, *Geophys. J. Int.,* **134**(2), 634–646.

Cassidy, J.F., 1992. Numerical experiments in broadband receiver function analysis, *Bull. seism. Soc. Am.,* **82**(3), 1453.

Christensen, N.I. & Mooney, W.D., 1995. Seismic velocity structure and composition of the continental crust: a global view, *J. geophys. Res.,* **100**(B6), 9761–9788.

Crotwell, H.P., Owens, T.J. & Ritsema, J., 1999. The TauP toolkit: flexible seismic travel-time and ray-path utilities, *Seismol. Res. Lett.,* **70**(2), 154.

Dettmer, J., Dosso, S.E., Cummins, P.R., Stipčević, J. & Bodin, T., 2015. Direct-seismogram inversion for receiver-side structure with uncertain source-time functions, *Geophys. J. Int.,* **203**(2), 1373–1387.

Green, P.J., 1995. Reversible jump Markov chain Monte Carlo computation and Bayesian model determination, *Biometrika,* **82**(4), 711–732.

Haskell, N.A., 1953. The dispersion of surface waves on multilayered media*, *Bull. seism. Soc. Am.,* **43**(1), 17–34.

Kennett, B. & Engdahl, E., 1991. Travel times for global earthquake location and phase association, *Geophys. J. Int.,* **105,** 429–465.

Kind, R., Kosarev, G.L. & Petersen, N.V., 1995. Receiver functions at the stations of the German Regional Seismic Network (GRSN), *Geophys. J. Int.,* **121**(1), 191–202.

Leahy, G.M., Saltzer, R.L. & Schmedes, J., 2012. Imaging the shallow crust with teleseismic receiver functions, *Geophys. J. Int.,* **191**(2), 627–636.

Lehujeur, M., Vergne, J., Schmittbuhl, J., Zigone, D. & Le Chenadec, A., EstOF Team, 2018. Reservoir imaging using ambient noise correlation from a dense seismic network, *J. geophys. Res.,* **123**(8), 6671–6686.

Licciardi, A. & Piana Agostinetti, N., 2014. High frequency receiver functions in the Dublin Basin: application to a potential geothermal site, *Energy Procedia,* **59,** 221–226.

Licciardi, A. & Piana Agostinetti, N., 2016. A semi-automated method for the detection of seismic anisotropy at depth via receiver function analysis, *Geophys. J. Int.,* **205**(3), 1589–1612.

Licciardi, A. & Piana Agostinetti, N., 2017. Sedimentary basin exploration with receiver functions: seismic structure and anisotropy of the Dublin Basin (Ireland), *Geophysics,* **82**(4), KS41–KS55.

Liu, G., Persaud, P. & Clayton, R.W., 2018. Structure of the northern Los Angeles basins revealed in teleseismic receiver functions from short-term Nodal seismic arrays, *Seismol. Res. Lett.,* **89**(5), 1680–1689.

Malinverno, A., 2000. A Bayesian criterion for simplicity in inverse problem parametrization, *Geophys. J. Int.,* **140**(2), 267–285.

Malinverno, A., 2002. Parsimonious Bayesian Markov chain Monte Carlo inversion in a nonlinear geophysical problem, *Geophys. J. Int.,* **151**(3), 675–688.

Malinverno, A. & Briggs, V.A., 2004. Expanded uncertainty quantification in inverse problems: hierarchical Bayes and empirical Bayes, *Geophysics,* **69**(4), 1005–1016.

Mooney, W.D. & Kaban, M.K., 2010. The North American upper mantle: density, composition, and evolution, *J. geophys. Res.,* **115**(B12).

Mosegaard, K. & Tarantola, A., 1995. Monte Carlo sampling of solutions to inverse problems, *J. geophys. Res.,* **100**(B7), 12431–12447.

Park, J. & Levin, V., 2016. Anisotropic shear zones revealed by backazimuthal harmonics of teleseismic receiver functions, *Geophys. J. Int.,* **207**(2), 1216–1243.

Piana Agostinetti, N. & Malinverno, A., 2010. Receiver function inversion by trans-dimensional Monte Carlo sampling, *Geophys. J. Int.,* **181**(2), 858–872.

Piana Agostinetti, N. & Malinverno, A., 2018. Assessing uncertainties in high-resolution, multifrequency receiver-function inversion: a comparison with borehole data, *Geophysics,* **83**(3), KS11–KS22.

Piana Agostinetti, N. & Martini, F., 2019. Sedimentary basins investigation using teleseismic P-wave time delays, *Geophys. Prospect.,* doi:10.1111/1365-2478.12747.

Piana Agostinetti, N., Martini, F. & Mongan, J., 2018. Sedimentary basin investigation using receiver function: an East African Rift case study, *Geophys. J. Int.,* **215**(3), 2105–2113.

Romero, P. & Schimmel, M., 2018. Mapping the basement of the Ebro Basin in Spain with seismic ambient noise autocorrelations, *J. geophys. Res.,* **123**(6), 5052–5067.

Saltzer, R., Leahy, G., Schmedes, J., Roth, J. & Rumpfhuber, E., 2011. Earthquakes—a naturally occurring source of low-frequency data, in *SEG Technical Program Expanded Abstracts 2011,* pp. 3689–3692.

Sambridge, M., Rickwood, P., Gallagher, K. & Jackson, A., 2006. Transdimensional inverse problems, model comparison and the evidence, *Geophys. J. Int.,* **167**(2), 528–542.

Shibutani, T., Sambridge, M. & Kennett, B., 1996. Genetic algorithm inversion for receiver functions with application to crust and uppermost mantle structure beneath eastern Australia, *Geophys. Res. Lett.,* **23**(14), 1829–1832.

Shiomi, K. & Park, J., 2008. Structural features of the subducting slab beneath the Kii Peninsula, central Japan: seismic evidence of slab segmentation, dehydration, and anisotropy, *J. geophys. Res.,* **113**(B10).

Thomson, W.T., 1950. Transmission of elastic waves through a stratified solid medium, *J. Appl. Phys.,* **21**(2), 89–93.

Wessel, P., Smith, W.H.F., Scharroo, R., Luis, J. & Wobbe, F., 2013. Generic mapping tools: improved version released, *EOS Trans. Am. Geophys. Union,* **94**(45), 409–410.

Yeck, W.L., Sheehan, A.F., Anderson, M.L., Erslev, E.A., Miller, K.C. & Siddoway, C.S., 2014. Structure of the Bighorn mountain region, Wyoming, from teleseismic receiver function analysis: implications for the kinematics of Laramide shortening, *J. geophys. Res.,* **119**(9), 7028–7042.

Zevallos, I., Assumpção, M. & Padilha, A.L., 2009. Inversion of teleseismic receiver function and magnetotelluric sounding to determine basement depth in the Paraná Basin, SE Brazil, *J. Appl. Geophys.,* **68**(2), 231–242.

SUPPORTING INFORMATION

Supplementary data are available at *GJI* online.

Please note: Oxford University Press is not responsible for the content or functionality of any supporting materials supplied by the authors. Any queries (other than missing material) should be directed to the corresponding author for the article.